PCCP

Accepted Manuscript

ROYAL SOCIETY OF CHEMISTRY

www.rsc.org/pccp

Segregation in Bimetallic Nanoparticles

Lingxuan Peng[1], Emilie Ringe[2], Richard P. Van Duyne[3], Laurence D. Marks[1]

[1]Department of Materials Science and Engineering, Northwestern University, Evanston, IL 60208

[2]Department of Materials Science & NanoEngineering, Rice University, Houston, TX, 77005

[3]Department of Chemistry, Northwestern University, Evanston, IL 60208

Abstract

Bimetallic nanoparticles are of interest due to their physical and chemical properties, which differ from their monometallic counterparts, and are dependent on size, composition and structure. Their unique chemical and physical properties make them useful in many optical, electronic and catalytic applications. In this perspective article we discuss segregation in bimetallic nanoparticles and highlight a recent analytical model based on minimization of energy. Computational approaches are discussed, along with a few examples and a comparison with the analytical approach. Experimental evidence for surface segregation is described, and finally, future directions are suggested. From this review of theoretical and experimental information it appears that a general consensus is starting to emerge that there are size-dependent variations in segregation in nanoparticles with the experimental data reasonably consistent with the theoretical models.

1. Introduction

Metal nanoparticles, typically 1 to 100nm, have been intensely studied in recent years. Due to their unique optical, electrical and catalytic properties, which different from their bulk counterparts, they are widely used in a variety of applications.[1-5] Bimetallic nanoparticles are of interest because the additional compositional degree of freedom enables tuning of the physical and chemical properties, which also depend on their size and structures.[6-12] One composition tunable attribute is the localized surface plasmon resonance (LSPR) in the UV-visible-NIR wavelength range.[6, 8] Noble metals such as Ag, Au or Cu are known to have unique optical properties, such as LSPR[13] and both theoretical and experimental works have shown that the localized surface plasmon resonance energy varies with the composition as well as the morphology of the alloy nanoparticles.[6, 8] A second property of interest is the catalytic behavior.[10, 12, 14-16] Bimetallic nanoparticles have been widely used in many reactions such as CO and alcohol oxidation, nitrogen oxide and organic molecule reductions, dehydrogenization reactions[10, 15] and show enhanced selectivity compared to their monometallic counterparts.[12, 17] It is established that the surface composition and surface segregation, i.e. deviation of the surface composition from the bulk, changes the chemical properties of the surface and the catalytic performances.[18-22] Compositional variations can also change which facets are exposed, which can be significant as different facets can have different catalytic activities and selectivities.[23-25]

The addition of the second element makes the structures of bimetallic nanoparticles much more complex than their monometallic counterparts. The two elements can be phase separated such as in core-shell structures,[26-28] chemically

ordered,[29-31] or Janus[32, 33] structures, or the two species can be randomly mixed with complex segregation.[34-36] The driving force for segregation is always thermodynamics, reduction in the total free energy of the particle. In many cases it is driven by surface and/or interface free energies, with a higher concentration of one element at the outermost surface monolayer or in the selvedge region stretching 1-2nm in from the surface. The reduction in surface free energy may be intrinsic to the element if the particle is in vacuum, or may involve additional energy gain by bonding to chemisorbed gas molecules or ligands. Strain energies can also play a role, and any initial structure produced by designed growth can be important, as will be the kinetics of segregation via diffusion. However, while it may be possible to fabricate more complex initial structures they will always over time transform towards the thermodynamically stable configurations – you can't beat Gibbs.

Most of these segregation processes are well known at the larger scale, but there is a subtle and important difference at the nanoscale. For a surface of a bulk material the large volume inside can act as a semi-infinite source or sink of atoms, so only the changes in surface components matter. In contrast, at the nanoscale the bulk volume is limited and the energy changes associated with changes in the bulk composition matter. This leads to new phenomena where the surface and bulk energy terms compete.

In this perspective, we focus on the segregation behavior of alloy nanoparticles. An analytical model describing the segregation behavior from a thermodynamic standpoint will be introduced in Section 2, followed by Section 3 with a brief discussion of the atomistic simulations used to predict segregation in bimetallic nanoparticles. In Section 4, some experimental results showing the segregation in bimetallic nanoparticle

via various characterization techniques will be discussed. Section 5 concludes this article with our perspectives, and proposes future work.

2. Analytical Models

The Wulff construction is the classic model describing the equilibrium shape of a free-standing single crystal particle as a function of orientation-dependent surface energies. It was developed by Wulff,[37] and later von Laue[38] gave a detailed mathematical explanation. More sophisticated proofs were provided by Dinghas[39] and Herring.[40] The construction uses the relationship that the plane normal h_i (the distance from the center of the particle to the facets) is proportional to the surface energy of the corresponding facet γ_i,

$$\mathrm{h}_i = \gamma_i / \Lambda \tag{1}$$

with Λ a size dependent scaling term. This model was subsequently extended by Marks[41] to include internal twin boundaries, and used to derive the thermodynamically stable shapes of multiply-twinned particles (MTPs). For supported particles extensions such as the Winterbottom[42] and the SummerTop[43] constructions (Fig. 1) were derived to incorporate substrate effects. For completeness, we note that if the particle is partially embedded in the substrate, the latter no longer constrained to be flat, there is no simple analytic solution currently known.

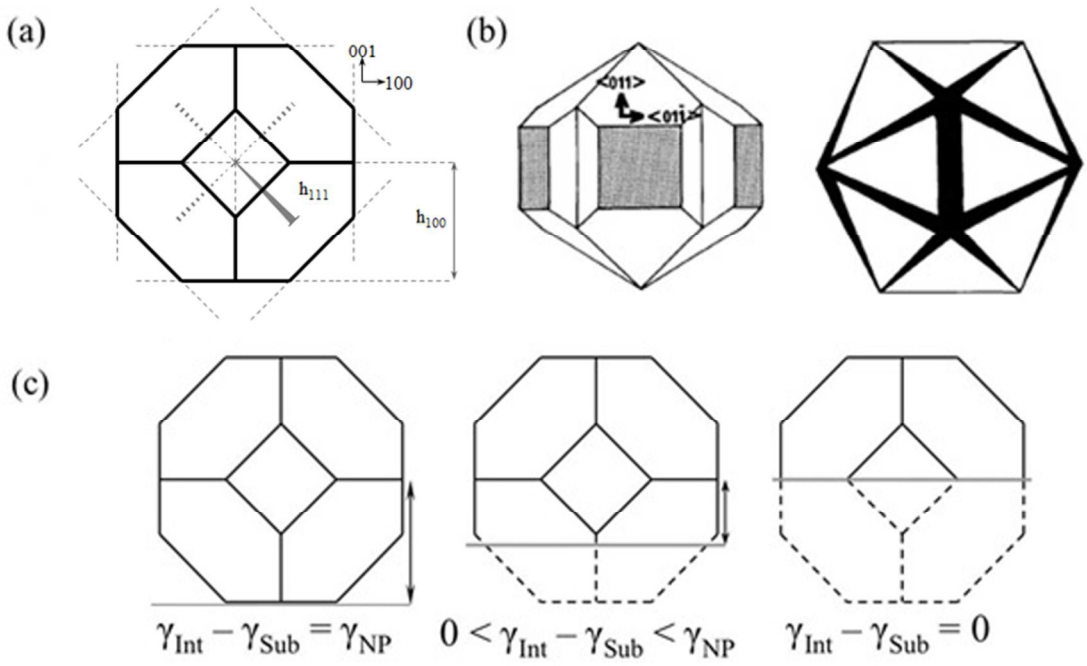

Fig. 1. (a) Conventional Wulff construction, (b) Modified Wulff construction, with twin boundaries introduced, (c) Winterbottom construction, with substrate effects included.

All the above constructions are exact for either free standing single crystals of a single stoichiometric compound or ones constrained to be on a flat substrate. However, if the material is not a line compound, i.e. there is a solubility range, these constructions do not include all the relevant terms. The key additional terms needed are those describing the bulk and surface compositions, as the variation of the free energy with composition is likely different for the two.

The simplest way to model alloys is to ignore the potential composition differences between the bulk and surface, what we will call the 'basic Wulff' approximation.[44] In this case both the bulk and surface energies are assumed to be equal to that of the homogeneous (initial) composition. It serves as a useful approximation for comparison purposes.

The next refinement of the model allows energy reduction through surface segregation, while ignoring changes in the bulk concentration. Here, the bulk is treated as an infinite reservoir; the change in bulk energy is neglected and the surface energy is calculated for a surface with an underlying composition equivalent to the homogeneous (initial) composition. Of course, this violates the law of conservation of mass, but it is an acceptable approximation, particularly for large systems.

However, for alloy nanoparticles with a small number of atoms, the infinite reservoir approximation is not valid, as the number of surface atoms can be comparable to the number of bulk atoms. The change in bulk energy due to segregation needs to be included. This is called the alloy Wulff construction.[44]

In the alloy Wulff model, the surface energy is assumed to vary as a function of composition. While this could be more complex, here we use a simple linear model and values taken from the literature.[44-49] For FCC metals, the surface energy of the (111) and (100) facets is significantly lower than that of the (110) and other higher order facets (AgAu, CuAu, and AuPd in Fig. 2). Regardless of initial concentration, the resultant lowest energy shape for a single crystal is between a cuboctahedron and an octahedron.

2.1 Analytical Solution of Alloy Particle Shapes

We will define some energy terms and will outline the solution for the shape of an alloy nanoparticle without strain when segregation is included.[44] The surface energy per unit area, $\gamma_{(n,C_1^S,C_1^V,C_2^S,C_2^V,\dots)}$, depends on surface fractional concentrations C_1^S, C_2^S,… and bulk fraction concentrations $C_1^V, C_2^V, \dots$, for elements 1, 2, … respectively, as well as crystallographic orientation, n, as below.

$$\gamma_{(n,C_1^S,C_1^V,C_2^S,C_2^V,\dots)} = \gamma_{(n,C_1^S,C_2^S,\dots)} + \tau\left(G_{(C_1^S,C_2^S,\dots)} - G_{(C_1^V,C_2^V,\dots)}\right) \quad (2)$$

where $\gamma_{(n,C_1^S,C_2^S,\dots)}$ is the free energy of a surface with orientation *n* and homogeneous concentration C_i^S for element i, τ is the thickness of the surface and G, the bulk free energy (plotted in Fig. 2).

The total size- and composition-dependent surface free energy is then the integral over all facets, E^S:

$$E^S = \int \left(\gamma_{(n,C_1^S,C_1^V,C_2^S,C_2^V,\dots)} + \sum \mu_i^S\left(x_i^S\right)\right) dS \quad (3)$$

where μ_i^S is the chemical potential of the surface and x_i^S is a small change in surface composition, defined as $d\gamma_{(n,C_1^S,C_1^V,C_2^S,C_2^V,\dots)}/dC_i^S$.

The change in bulk energy, ΔG, is the difference between the free energy per unit volume of the bulk concentration $C_1^V, C_2^V, \dots$ and initial (homogeneous) bulk concentration, $B_1^V, B_2^V, \dots$

$$\Delta \mathrm{G} = G_{(C_1^V,C_2^V,\dots)} - G_{(B_1^V,B_2^V,\dots)} \quad (4)$$

The total change in bulk energy E^V, is ΔG integrated over the particle volume, and the equilibrium shape found by minimizing the sum of E^S and E^V with respect to the change in surface and bulk concentration while conserving mass. The general solution can be written as follows:[44]

$$\frac{\gamma_{(n,C_1^S,C_1^V,C_2^S,C_2^V,\dots)}}{\{\Lambda - \Delta G\}} = h_{(n)} \quad (5)$$

where $h_{(n)}$ is the magnitude of the face-dependent surface normal, n is the crystallographic orientation, and Λ is the Wulff constant as in the conventional Wulff construction.

Eqn (5) is analogous to the conventional Wulff construction (Eqn (1)). Setting ΔG to zero yields the simpler 'infinite reservoir' model; ignoring the composition variation of everything yields the basic Wulff construction. We note that similar to the Winterbottom and Summertop constructions, interfaces can be included in Eqn (5) directly.

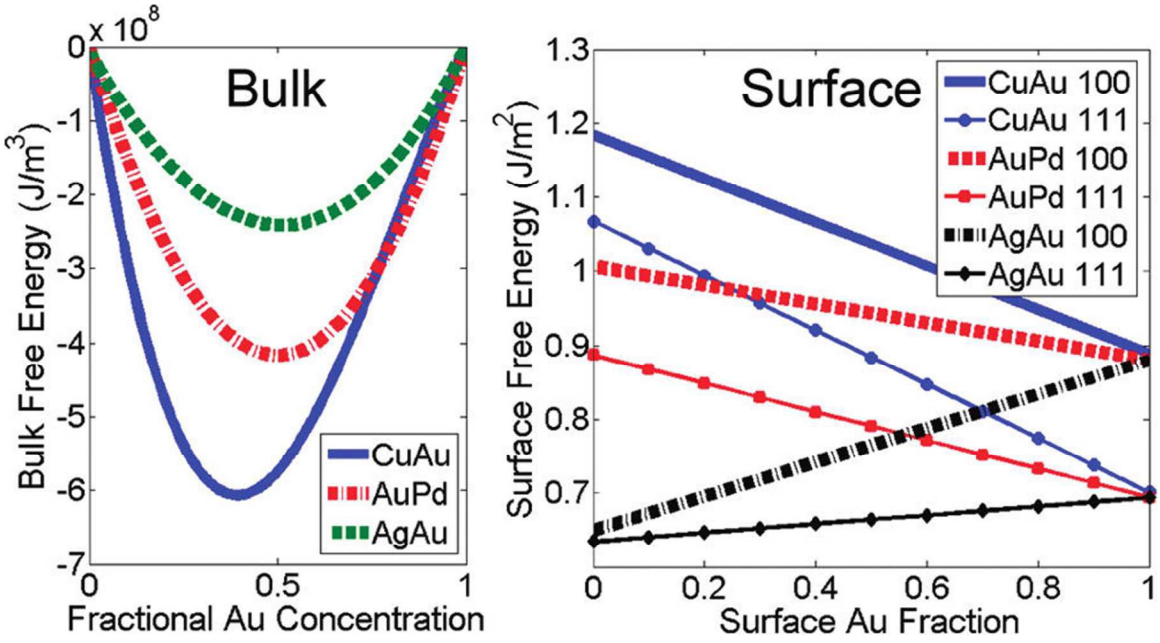

Fig. 2. Fitted bulk and surface free energy for CuAu, AuPd, and AgAu. The bulk free energy is defined as the deviation from the linear interpolation between two pure elements. The surface free energy is assumed to vary linearly between two pure surfaces.

2.2 Size-dependent Segregation in Alloy Wulff Construction

Unlike the case for a single line compound nanoparticle, surface segregation, as well as the equilibrium shape of the particle, will depend on the size of the particle, as ΔG is size dependent. Independently, surface segregation is energetically favorable. However, the free energy increase due to the bulk composition change opposes this

energy reduction. The competing terms, in conjunction with size and composition, yield a range of possibilities as described below.

The first case to consider is "strong" alloys, for which the largest deviation from the linear interpolation of the bulk energy is greater than 1%. AuCu[12, 44, 45, 47, 48] and AuPd,[44, 46, 50] with approximate maximum deviations of 1.2% and 1.1%, respectively, both fall into this category. In these two alloys, the energy gain from segregation is larger than the cost in bulk energy. When the homogeneous concentration of Au is small, referred to as regime 1, all the Au atoms go to the surface, although there may not be enough Au atoms to form a monolayer. The bulk concentration change is more significant when the particle is very small, so regime 1 is most significant when the number of atoms is fewer than 10^4, approximately 7 nm in diameter. As the overall (homogeneous) Au concentration increases, the energy gain through segregation becomes comparable to the energy cost in the bulk, leading to regime 2. Lastly, at high homogeneous Au concentration, the bulk energy cost can no longer prevent the formation of a pure Au surface, and regime 3 begins. The three regimes are marked in Fig. 3. The size-dependence of this transition is negligible for particles with more than 10^5 atoms, approximately 15 nm in diameter.

The second case is "weak" alloys, for which the maximum deviation is less than 1%. i.e. ~0.65% for AgAu.[44, 45, 51, 52] Here, ΔG is small, so the surface component dominates for all concentrations. All available Ag atoms will segregate towards the surface until a pure Ag surface is achieved. If there is a surplus of Ag, the bulk will be alloyed. Segregation in such "weak" alloys is also size-dependent, mainly due to the decreasing surface-to-volume ratio with increasing particle diameter.

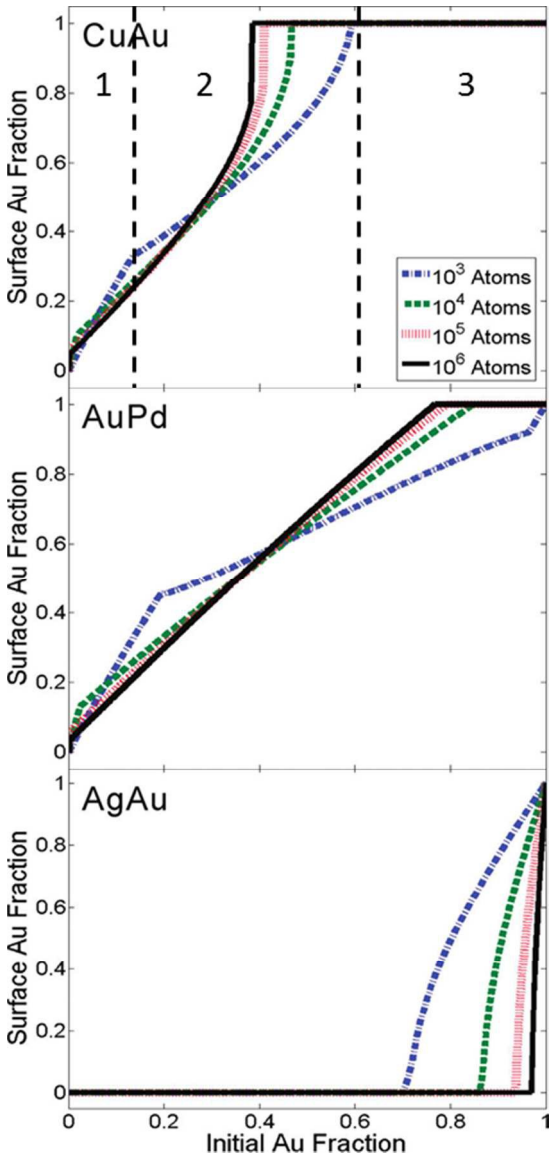

Fig. 3. Effect of size and initial composition on the equilibrium surface composition of alloy particle. Curves for 10^3, 10^4, 10^5 and 10^6 atoms (~3, 7, 15 and 30 nm in diameter) are plotted as a function of overall composition. The three regimes can be observed in CuAu and AuPd particles, while only two regimes can be seen for AgAu.

2.3 Equilibrium Shape of Alloy Nanoparticles

The shape of the particle, which can be parameterized by the ratio of the surface normal of the (111) and (100) facets, h_{111}/h_{100}, varies with both size and composition.

In the basic Wulff model, the h_{111}/h_{100} ratio is constant. In the 'infinite reservoir' model it varies with composition, but not with size. In the alloy Wulff model, the shape

changes with both size and composition, with derivative discontinuities at the boundaries of the three different regimes as shown in Fig. 4. While the differences in the ratio of surface normal h_{111}/h_{100} for particles of different sizes are small, the surface area ratio S_{111}/S_{100} changes drastically. For instance, in 3000 atom and 1000 atom AuCu alloy particles with an initial Au fraction of 0.15, the surface normal ratios are 0.86 and 0.84, respectively, while the surface area ratios are 1.9 and 2.4 respectively.

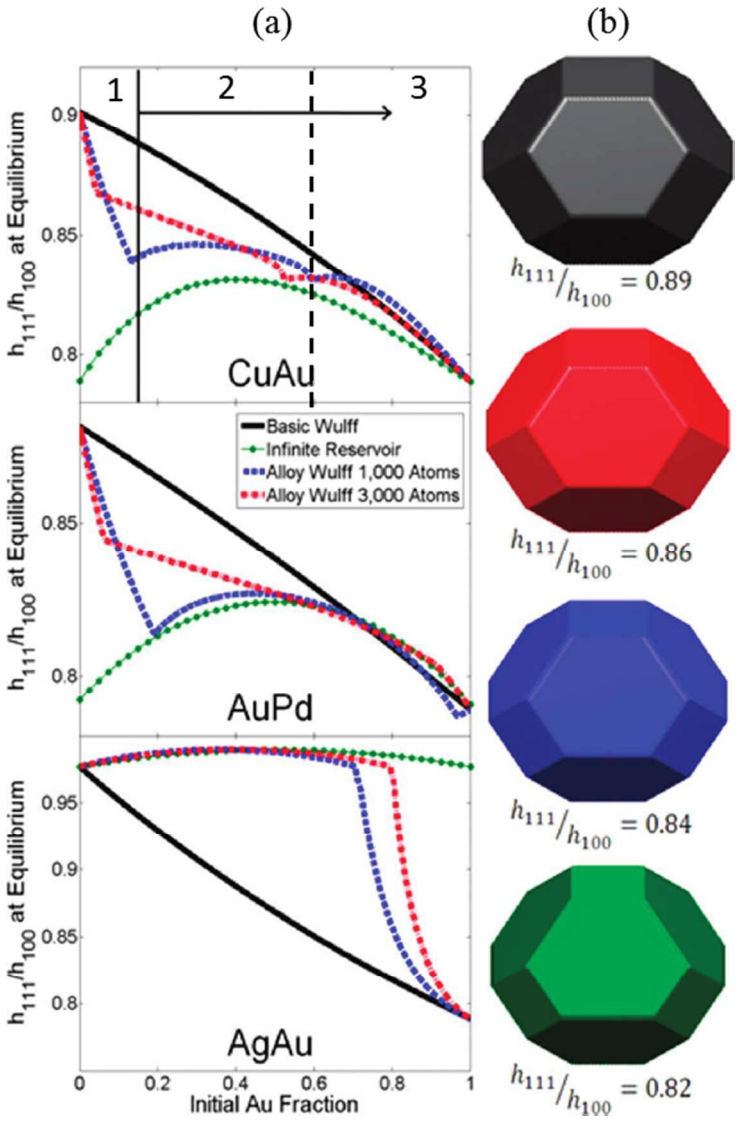

Fig. 4. Shape dependence on size and homogeneous composition of the particles, parameterized by (h_{111}/h_{100}). (a) Shape as a function of homogeneous composition of Au for 'basic Wulff' model (black), 'infinite reservoir approximation' (green) and alloy

Wulff model for two particle sizes (blue for 1000 atoms, red for 3000 atoms). (b) Shape variations of CuAu alloy particles with a homogeneous Au concentration of 0.15, according to respective models.

2.4 Temperature-dependent Surface Segregation

The surface segregation and equilibrium shape will also depend on temperature, since the competing free energy terms discussed in section 2.2 are a function of temperature. To investigate this we will neglect the temperature-dependence of the enthalpy of mixing, assuming its contribution to the free energy is small compared to the entropy of mixing term, which is linear with temperature (T).

A reasonable form for the temperature dependence of surface energy was derived by Kristyan and Giber[53] based on statistical mechanics. The partial derivative of surface energy γ respect to temperature T $\frac{\partial \gamma}{\partial T}$ is materials dependent and can be written as,

$$\frac{\partial \gamma}{\partial T} = -Rln(m) \tag{6}$$

where R is the gas constant; m the number of surface layers which is dependent on materials.

This temperature dependence can be expanded for an alloy,

$$\frac{\partial \gamma}{\partial T} = \frac{\partial \gamma_B}{\partial T} + x(A)\left(\frac{\partial \gamma_A}{\partial T} - \frac{\partial \gamma_B}{\partial T}\right) \tag{7}$$

and the temperature dependent surface energy is then as follows

$$\gamma(x,T) = \gamma_o(x) - R\left[lnm_B + xln\left(\frac{m_A}{m_B}\right)\right]T \tag{8}$$

where $\gamma_o(x)$ is the surface energy as a function of surface composition at 0K. Therefore, the change in surface energy at temperature T is

$$\int \left\{ \left(\gamma_o(x^S) - \gamma_o(x^H)\right) - RT\left[(x^S - x^H) ln \frac{m_A}{m_B}\right] \right\} dS \tag{9}$$

while the change in bulk energy is

$$\int RT\left[x^V lnx^V + (1 - x^V) ln(1 - x^V) - \left(x^H lnx^H + (1 - x^H) ln(1 - x^H)\right)\right] dV \tag{10}$$

where x^S is the surface composition of element A, x^H is the homogeneous composition of the alloy, x^V is the bulk composition of element A after segregation.

The contribution to the free energy from the entropy of mixing is minimal at low temperature but will dominate at high temperature with the entropy of mixing driving the particle toward homogeneity. This leads to an unresolved issue: when one compares analytical models with experimental data and sometimes numerical models; to what extent do these predictions represent quenched structures as opposed to the thermodynamically stable ones?

3. Numerical Models of Nanoalloy Segregation

The analytical alloy Wulff construction gives valuable information as to how size, shape, temperature and composition affect the segregation in bimetallic nanoparticles. However, there are free variables in the model, so it is not always apparent how segregation will occur in specific cases. Here, it can be useful to use numerical approaches to model specifics, with potentials or similar, that represent the details of the system. Most of these use computational methods of finding the global minimum of the potential energy surface (PES), which is the configurational energy of the cluster as a function of the atomic coordinates.[54] They can be divided into two categories, first-principles methods and empirical/semiempirical methods. First-principles methods, also

known as *ab initio* methods, are very informative, and they yield relatively accurate energies. However, they are very computationally demanding and thus only can be applied to systems of limited size.[55, 56] Empirical/semiempirical methods involve a system dependent potential[57-62] that can be of various forms. These models allow more efficient calculations thus enable calculations for larger systems. In many cases, the simulations use both DFT and empirical/semiempirical approaches, and apply a global optimization method. There are several recent reviews on global optimization of alloy clusters utilizing different algorithms/methods.[54-56, 63]

In the next sections we will briefly outline the main methods that have been used, including a few results where we can compare the conclusions of the numerical methods with the analytic models. In general the two appear to be quite consistent.

3.1 Computational Methods

3.1.1First-principles Methods

The most direct method to determine the lowest energy structure is via first-principles calculations, such as density functional theory (DFT). However, the number of possible structures to be evaluated using first-principles techniques increases rapidly with particle size, given that the number of possible structures is (A+B)!/A!B!, where A and B are the numbers of A and B atoms, respectively. Thus using DFT calculation to directly search for lowest energy structure is only feasible for particles with few atoms.[55, 56] However, in order to perform DFT calculations on bigger particles, a hybrid approach can be used. The DFT optimization can be performed on a set of local minima obtained by global optimization utilizing empirical potentials. A few recent articles have given reviews on this topic.[56]

DFT methods are powerful because rigorously they only involve one approximation, the exchange-correlation energy functional, E_{XC}, which is a linearization of the underlying many-body electron problem, although often other approximations are made so the calculations are less computationally demanding. Since the position of the atoms does not depend much upon approximations made in this functional, with most modern variants being accurate to about 1%, DFT methods are good for determining structures and can also handle non-equilibrium properties, such as activation energy barriers to diffusion, reasonably well. One caveat is that they can be quite bad for surface enthalpies. The earliest functional to be used was the localized-density approximation (LDA, e.g. [64]). While LDA can sometimes give relatively good surface energies and other results due to a fortuitous cancellation (e.g. [64-66]) the failings of the LDA are now well established. The most common functional currently used is the Perdew-Burke-Ernzerhof Generalized Gradient Approximation (PBE GGA), [67] which, while it often gives very good results, still has some problems, particularly for surface energies. For instance, it is now well established that it severely underestimates surface energies [68-70] in many cases. In conclusion, DFT methods are good, but not infallible.

3.1.2 Empirical and Semi-empirical Methods

For larger scale calculations typical approaches are empirical or semiempirical. Many-body potentials, such as second-moment approximation tight-binding (SMATB) potentials,[61, 62] embedded-atom method (EAM)[57, 71] potentials and later Gupta,[59] Rosato-Guillope-Legrand,[61] Sutton-Chen[58] potentials have been used to calculate the total energy of the cluster. Some Modified Embedded-atom Method[72] (MEAM) potentials have been widely used in recent years. The choice of the potential is strongly system dependent.

One caveat with these methods is that unlike DFT, they employ potentials fitted to reproduce some known properties of the material, such as elastic constants and heat of formation. While they can be very accurate for the ground state, properties such as the activation energy barriers can be harder to include accurately. Since there is only limited knowledge of how these properties vary with systems in all cases, obtaining a viable parameterization that includes them accurately can be problematic.

3.1.3Global Optimization

The most popular global optimization approaches are via genetic algorithms [55, 63, 73] (GA) and basin-hopping[74] (BH) methods. Genetic algorithms are a widely used global optimization method based on evolutionary principles where the number and positions of atoms is reduced to a binary code. Starting with an initial random population of bit strings (structures) they are energetically minimized and sorted with respect to a fitness value, such as the energy. By a probabilistic approach based upon the energy, and in some cases more advanced strategies such as similarity (see[73] for details) pairs of bit strings are joined similar to combining genes during evolution. A new population of particles is produced, which are then optimized. This procedure is run for a number of cycles and a record kept of the best structures found. With care this algorithm samples the full potential energy surface and will find the local minima, not just the global minima. The method works because it finds rapidly favorable combinations of bits (atomic positions), which are called schema, so is well suited for looking at permutations of site occupancies in alloys.

Basin-Hopping is a Monte Carlo method[74] based on statistical mechanics, with the Metropolis algorithm often chosen for the simulations.[56, 75] The positions of randomly

chosen atoms A and B are exchanged, and the total energy of the system before and after atom exchange calculated based on the potential used. If the change of energy ΔE is negative, the exchange is favored and thus accepted. On the other hand, if ΔE is positive, the exchange will be accepted by a probability of $\exp(-\Delta E/k_B T)$, where T is the temperature used in the simulation. A number of recent studies on segregation in bimetallic nanoparticles have been performed by this approach. [75-79]

3.2 Examples of Alloy Segregation

A few representative examples focusing on surface segregation will be discussed here, comparing the numerical results with the earlier analytical models. Wang *et al.* [80] investigated Pt surface segregation in Pt_3Ni, Pt_3Re and Pt_4Mo cuboctahedral bimetallic nanoparticles. A MEAM potential and a Monte Carlo method were used to obtain the equilibrium state of the particles. The segregation is strong in Pt_3Re and Pt_3Ni and relatively weak in Pt_4Mo, and the segregation in all three systems was size-dependent. The size-dependent segregation is shown in Fig. 5 (a), (b) and (c). Our interpretation is that at smaller sizes, not as many Pt atoms segregate to the surface, consistent with the analytical model. Due to the large lattice parameter difference between Pt and Ni atoms, a tendency to form chemically ordered structures was observed. The atomic images of Pt_3Ni, Pt_3Re and Pt_4Mo cuboctahedral bimetallic nanoparticles can be found from ref 80. Similar results were also observed in simulations of PdAg, CuAg, AuPt and NiAg systems *etc.*[76, 81] In Pt_4Mo particles, the preferential segregation of Pt was to the facets, rather than edge and corner sites, with alternate Mo and Pt atoms. One caveat we note is that the simulations were restricted to cuboctahedral shapes, which may not be the equilibrium shape.

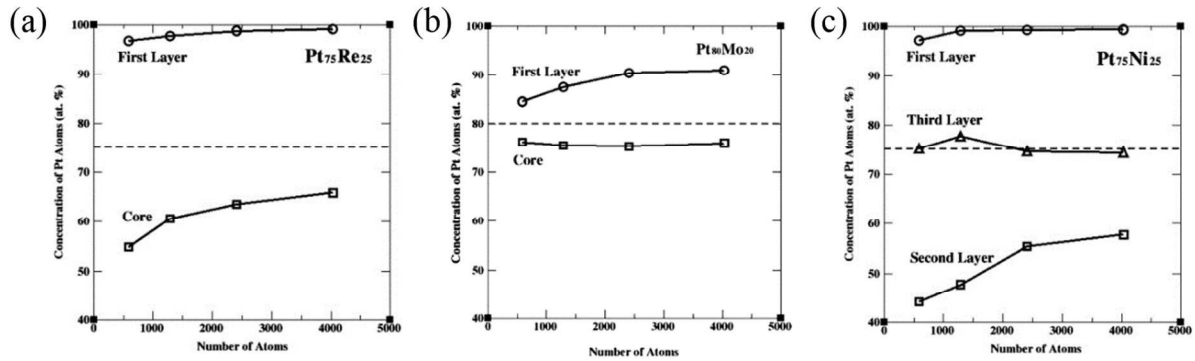

Fig. 5. (a-c) The calculated Pt fraction on the surface layer and in the core region as a function of size in (a) Pt_3Re and (b) Pt_4Mo particles at 600K. The dashed line shows the overall Pt concentration in the particle. (c) The calculated Pt fraction in the first three layers as a function of size in Pt_3Ni particles at 600K. The dashed line shows the overall Pt concentration in the particle. Reproduced with permission from Ref. 80.

In other work Deng *et al.* [76] analyzed site-selective segregation utilizing Monte Carlo methods. Taking $AuPt_3$ as an example, the surface composition of Au increased with particle size. By performing Monte Carlo simulations at different temperatures, it was found that the surface segregation was not as significant at higher temperatures. Both the trend of segregation with size and the reduction of segregation with temperature were consistent with the earlier analytical model. Interestingly, competitive multisite segregation (site-preferential segregation) was also observed. The Au atoms preferentially segregated at the vertices, edges and (100) facets, rather than (111) facets, as the decrease in configurational energy when switching Au and Pt atoms at surface sites with different coordination numbers (i.e. vertex, edge, (100) facets and (111) facets), is not the same. This is the standard term in an entropy analysis for the multiplicity of certain types of sites. Pt atoms preferentially segregate to sites with lower coordination numbers because the magnitude of configurational energy change is larger at these sites. The surface Au composition changed as a function of total Au composition in the particle as shown in Fig. 6. For completeness, when the composition of Au was high, the

equilibrium configuration had a three-shell structure similar to the earlier chemically ordered case. Including all these factors in analytical models is difficult, although atomistic calculations are particularly powerful for extracting details at the atomic scale.

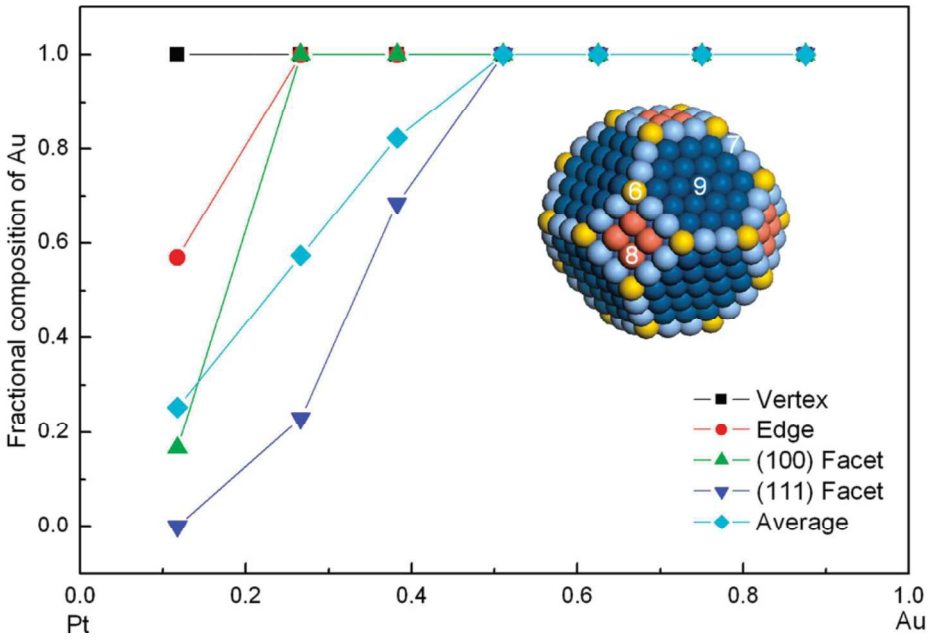

Fig. 6. Composition fraction of Au at different sites (vertex and edge) and facets ((100) and (111)) as a function of overall Au composition for particles containing 586 atoms. Reproduced with permission from Ref. 76. Copyright 2010 American Chemical Society.

Nanoparticles are often deposited onto an oxide or carbon-based substrate to form heterogeneous catalytic systems.[5, 82-84] In many cases, the substrate plays an important role in the catalytic reactions. The presence of a substrate also influences the structure of supported bimetallic nanoparticles. [85] As an example, Negreiros *et al.*[86] performed EP-DFT calculation showing that the interface between AgPd nanoparticles and MgO (100) substrate was Pd-enriched while the surface of the particle was Ag-enriched. The Pd enrichment at the interface was attributed to the stronger Pd-O bond compared with the Ag-O bond. The fraction of Ag atoms at the interface increases with the cluster size. The lattice mismatch between Pd (100) and the O-O distance of MgO (100) is larger than that of Ag. Thus, Ag helps release the stresses at the interface. The presence of the support

not only affected the interface segregation, but also influenced the most stable shape and structure of the supported particles. For pure Ag and Pd, the particles favored cube-on-cube epitaxy. In AgPd with 50% Ag composition, the energy predicted by empirical potentials showed that the decahedral (Dh) shape was also a stable structure for AgPd supported particles, as opposed to pure Ag or Pd supported particles, for which the energy was high. Single crystal FCC (111) on MgO (100) had a comparable energy to Dh and FCC (100) structures for particles with a size of 400 atoms. We suspect that there could be mixed epitaxy in this case. Pd enrichment at the interface was also predicted for the AuPd on MgO (100) system. The epitaxy is good for small Pd-rich particles, but when the size or/and Au composition increases, there are larger strains.[87]

4. Experimental Evidence of Segregation in Bimetallic Nanoparticles

While, theoretical methods are very useful to predict the segregation behavior in bimetallic nanoparticles, experiments are critical to validate and challenge these models. Here we present selected studies from the wide variety of approaches available to characterize bimetallic nanoparticles, such as mass spectrometry, microscopy, diffraction and different types of spectroscopies.[9, 54]

4.1 Electron Microscopy

Because of its ability to detect composition at the sub-nm level, transmission electron microscopy (TEM) is one the most direct and accurate techniques to gather information on the size and structure of nanoparticles. TEM is particularly powerful in imaging and analyzing the local chemical composition distribution, such as any phase separation or segregation, as shown in the examples below.

4.1.1 High-angle Annular Dark Field Imaging in Scanning Transmission Electron Microscope (HAADF)

The modern high-resolution scanning transmission electron microscopy is a powerful tool to study the local compositional distribution in bimetallic nanoparticles, in combination with energy dispersive X-ray spectroscopy (EDX) and electron energy loss spectroscopy (EELS). HAADF imaging, sometimes referred as Z-contrast imaging, is often used in bimetallic systems.[27, 35, 88] This type of image is formed by collecting the high-angle, incoherently elastically scattered electrons, as a function of probe position, with an annular detector positioned after the sample. The contrast in HAADF imaging is directly related toZ^{α}, where Z is the atomic number and α is a constant ranging from 1.5 to 2, depending on the collection angle. α approaches 2 when the collection angle is high and most of the Bragg reflections are avoided.[89, 90] This technique is particularly useful for bimetallics with a large atomic number difference, e.g. the promising catalysts Cu-Au, Au-Pd, Au-Ag, and Ni-Au. [88, 91-98]

Recent HAADF images of NiAu bimetallic nanoparticles taken using an aberration corrected STEM are shown in Fig. 7.[88] The heavier Au is easily distinguishable from the Ni, thus the local, intra-particle composition variation can easily be observed.

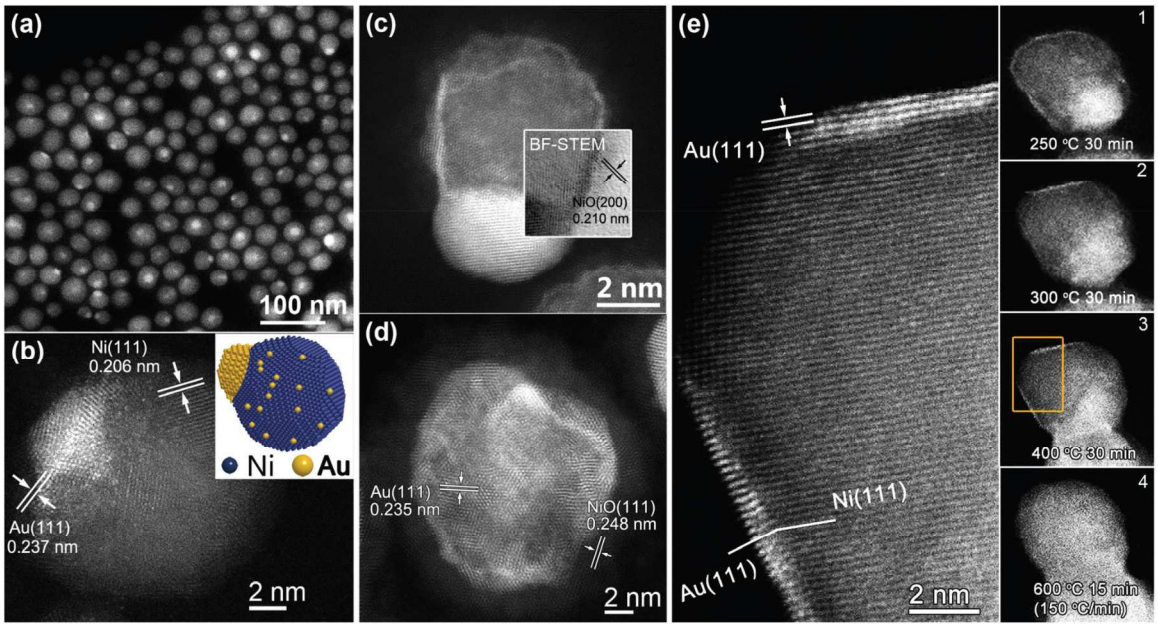

Fig. 7. High-angle annular dark field (HAADF) images of NiAu bimetallic nanoparticles (a) as synthesized NiAu nanoparticles at low magnification (b) as synthesized NiAu nanoparticles at high magnification, with an inset of the corresponding schematic model (c) NiAu particle oxidized in air for 85 days with an inset of a ABF image at the same area (d) oxidized NiAu particle annealed in air for 8 hrs and (e) *in-situ* vacuum annealed NiAu nanoparticles; the four insets show the particle structure at different temperatures. Reproduced from Ref. 88 with permission from The Royal Society of Chemistry.

4.1.2 Energy-dispersive X-ray Spectroscopy (EDX)

Energy-dispersive X-ray Spectroscopy (EDX) is often used to reveal the compositional distribution in bimetallic nanoparticles. The EDX detector collects the element-specific characteristic X-rays emitted, as a function of probe position.[99] EDX can only identify elements heavier than Beryllium and is particularly sensitive to heavier elements. The spatial resolution of EDX depends on a number of factors, including the electron beam voltage, and the sample thickness (particle size). With modern aberration-corrected microscopes it approaches atomic resolution, and by using tomographic methods, i.e. collecting spectra with many different beam directions, it can provide 3-D chemical information. [100]

4.1.3 Electron Energy Loss Spectroscopy

Electron energy loss spectroscopy (EELS) mapping can also be utilized to reveal elemental distribution. EELS offers better spatial and energy resolution than EDX and is capable of providing elemental information as well as electronic and bonding information.[99] A number of factors, such as the incident-beam energy, collection semi-angle and the energy dispersion control the resolution; typically it is better for light elements. With the best microscopes, resolution can be on the atomic scale, ~0.2nm, and under ideal circumstances, as low as 0.1nm.

4.1.4 High-resolution Transmission Electron Microscopy

High-resolution transmission electron microscopy (HREM) has been able to image nanoparticles at the Angstrom scale for many years,[101-104] and modern aberration corrected microscopes have picometer precision,[105] but it is difficult to obtain the elemental information directly. To aid interpretation, HREM is usually coupled with HREM image simulation. In a recent study,[106] Pohl *et al*. used HREM with a combination of molecular statics, Monte Carlo and HREM image contrast simulation, to demonstrate the segregation of Pt atoms to the surface of icosahedral FePt particles.

4.2 Experimental Evidence of Segregation in Bimetallic Nanoparticles

Usually the characterization techniques listed above are used in combination. Below we describe a few of the recent studies focusing on segregation in bimetallic nanoparticles.

Suntivish[19] *et al* showed that there was a correlation between surface compositions and electrocatalytic activities of bimetallic nanoparticles. The as-synthesized PtAu particles with Pt-rich (90% Pt) surfaces were annealed at 500°C in Ar. The Au atoms were observed to migrate to the surface, with a final surface concentration

of 87% Au. We believe that the Au is segregating to reduce the surface energy, consistent with the results discussed above. The same as-synthesized particles were also annealed at 250°C in air. In this case, the Au atoms still migrated to the surface, although not to the same extent as the particles annealed at 500°C in Ar, while the surface remained Pt-rich (68% Pt). It was claimed that a high temperature was necessary to remove surfactants, which were stabilizing the surface Pt. 250°C was shown to be the lower limit of the temperature range required for segregation to take place. A comparative experiment was done on particles which were annealed at 250˚C in Ar, where no noticeable surface segregation was measured, perhaps because fewer surfactant molecules were removed in Ar. We suspect that the surfactants lower the relative surface energy of Pt compared to Au. Particles further annealed in Ar at 350˚C, showed Au migration to the surface. EDX linescans and maps are shown in Fig. 8. These results appear to be quite consistent with the theoretical models of alloy segregation.

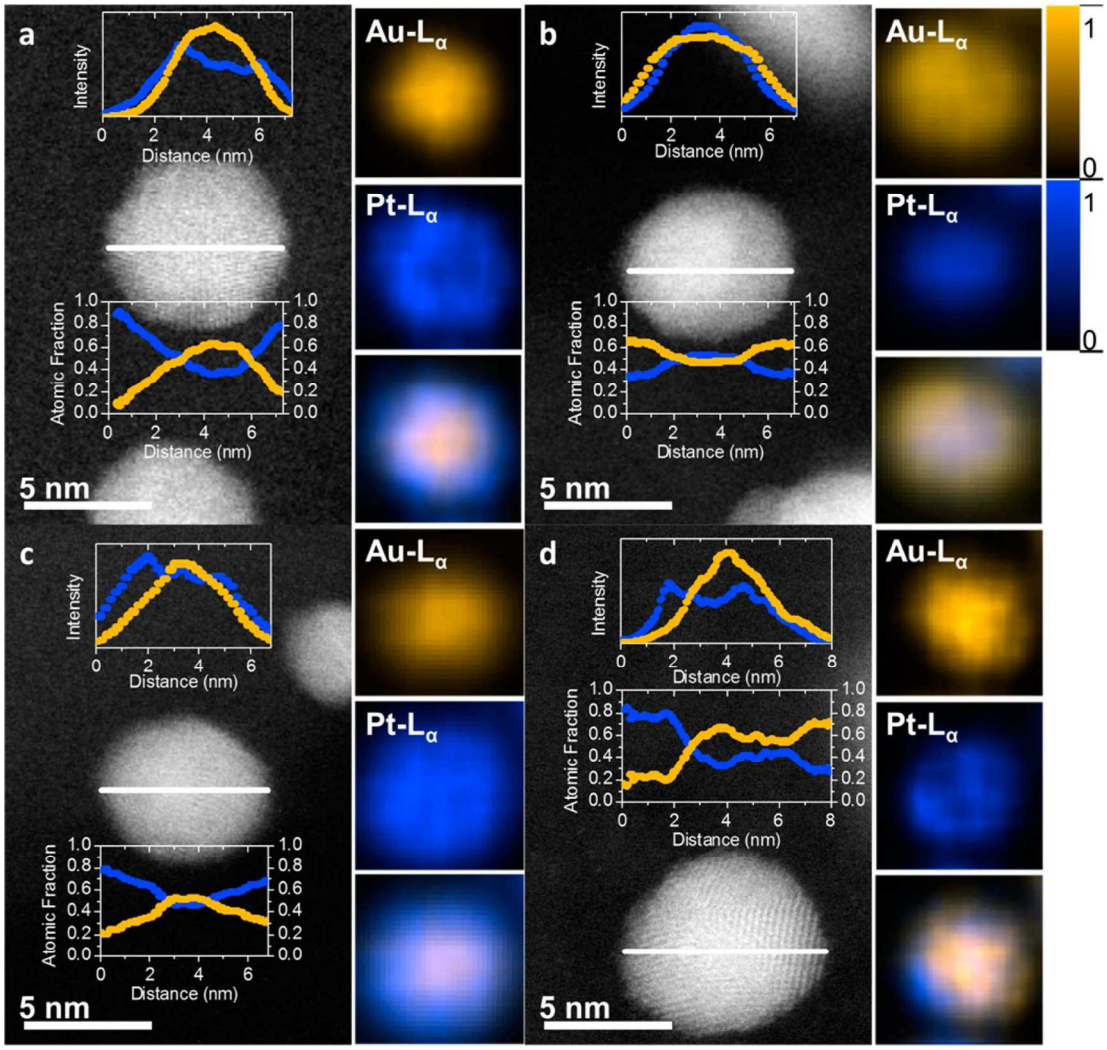

Fig. 8. Aberration-corrected STEM annular dark field (ADF) images and EDX of AuPt bimetallic nanoparticles. (a) As-synthesized particles (90% surface Pt) (b) Heat treatment at 500°C in Ar for 30 mins (13% surface Pt) (c) Heat treatment at 250°C in air for 30min (68% surface Pt) (d) Heat treatment at 250°C in air for 30min, followed by heat treatment in Ar at 350°C for 30min (30% surface Pt). The ADF images with EDX linescans are shown in the left, and the right shows the EDX mappings of these particles. The colors were universally scaled. Reprinted with permission from Ref. 19. Copyright 2013 American Chemical Society.

Some theoretical studies have been able to show site-selective segregation[76, 107] in bimetallic nanoparticles. Cui *et al.* found that in Pt_xNi_{1-x} alloy nano-octahedra, the Ni atoms preferentially segregate to the (111) facets, while Pt prefers the edges and corners, resulting in a Pt-rich frame.[35] The HAADF images and EELS linescans and mappings in

Fig. 9 show the compositional distribution of Pt and Ni in the PtNi nanoparticles of different composition ratio. Pt-rich frame features have also been found in polyhedral.[108] Chen *et al*. have exploited this feature to synthesize open structure Pt_3Ni nanoframes.[108] These site-selective segregation studies are of interest in the design of new nanoparticle morphologies.[107] Open structures, with their high surface to volume ratio, may be of use as electrocatalysts, and selective etching of site segregated particles can produce novel structures.[107, 108] The alloy Wulff model lacks the ability to predict such atomistic details, but they can be revealed by numerical simulation.

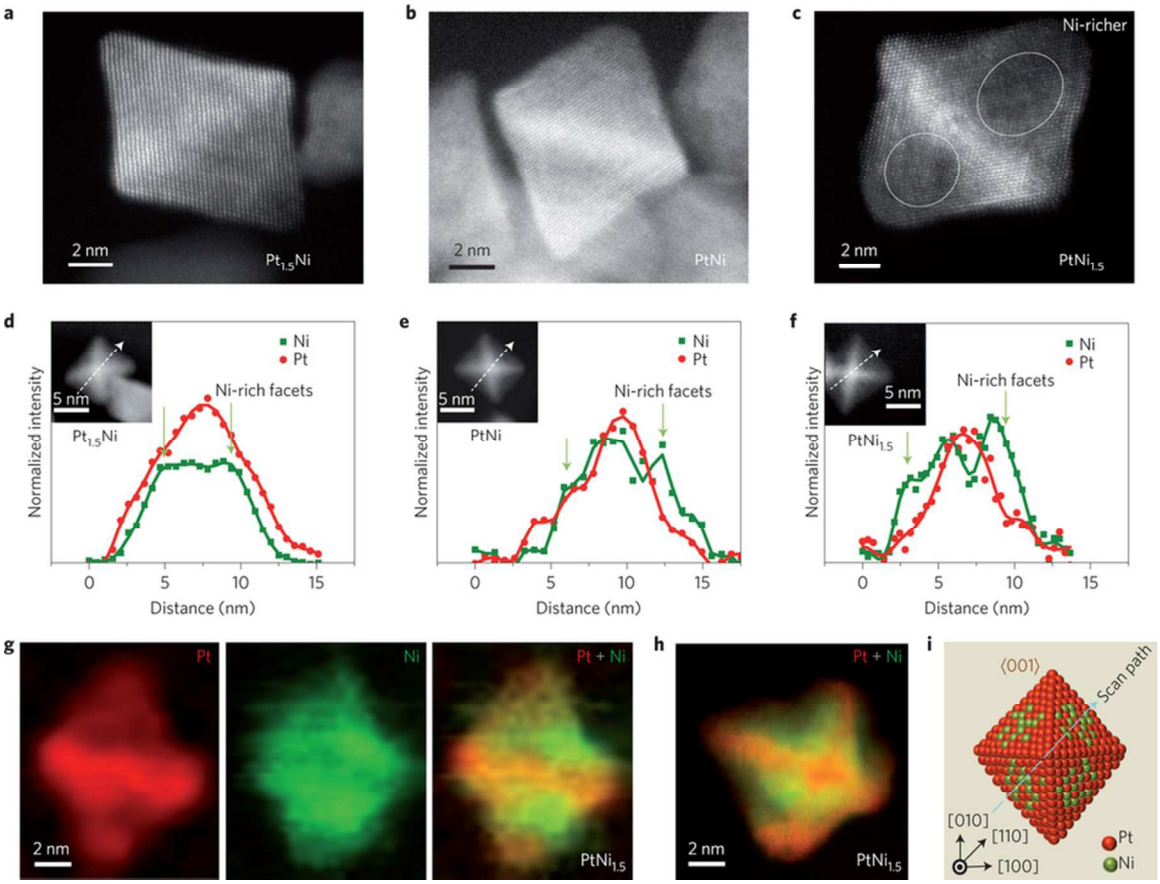

Fig. 9. Atomic-resolution z-contrast images, EELS lines and mappings of Pt_xNi_{1-x} octahedral nanoparticles. (a-c) Z-contrast images of octahedral particles close to <110> zone axis of (a) $Pt_{1.5}Ni$, (b) PtNi, (c) $PtNi_{1.5}$. (d-f) EELS linescans of octahedral nanoparticles close to <100> zone axis of (d) $Pt_{1.5}Ni$, (e) PtNi, (f) $PtNi_{1.5}$. The linescans are along the [110] direction, passing through the longest axis. The insets are the z-contrast images of the corresponding particles. (g) EELS elemental map of $PtNi_{1.5}$ octahedral nanoparticle showing preferential segregation of Ni (green) to the (111) facets, and Pt (red) enriched edges and corners. (h) A composite image of a HAADF image showing Pt red, and an EELS elemental map showing Ni green. (i) Ball schematic showing the octahedral particle along the <001> zone axis, with Ni-rich facets and Pt-rich frame. Reproduced with permission from Macmillan Publishers Ltd: Nature Materials Ref. 35, copyright 2013.

5. Perspective

From the brief survey of both experimental and theoretical studies to date regarding segregation in nanoscale alloys, there appears to be a general consensus on some aspects. Broadly, the predictions of the analytical continuum approach are supported by both atomistic theoretical models and experimental data. However there are

fine details which were not included in the original analyses and appear to be better handled via atomistic approaches. Such details include segregation to edges and corners, versus flat surfaces, and ordered phases. It is fair to state that at a size scale of 10^3 atoms or less (perhaps in some cases 10^4 atoms), the infinite reservoir approximation is not valid, and there can be quite dramatic particle size effects on the Wulff shape and equilibrium segregation.

The alloy Wulff construction above is valid for single crystal alloy nanoparticles. However, in real experiments, particles are not always single crystals, but may be multiply-twinned particles (MTPs) containing several twin boundaries, such as decahedra (Dh), containing five single crystal segments, and icosahedra (Ic), containing twenty single crystal segments. Due to the fact the single crystal segments are not completely space filling in either case, there are some strain fields associated with the MTPs, which have been considered in several ways.[109-113] Ino[111] modeled the strain term as homogeneous strain. Later, de Wit[113] modeled this term as inhomogeneous strain via the Volterra disclination[114] model. Marks, Howie, and Yoffe[115] further analyzed the inhomogeneous strain and have given the analytical solutions for both Dh and Ic. In such cases there can be substantial segregation of large atoms to the surface and small atoms to the center of the particle.[116]

To further extend the shape modeling, a few more factors can be taken into consideration. The degree of segregation in alloy Wulff construction was assumed to be the same for different facets. However, this need not be the case as face-dependent segregation or equilibrium with a gas species can readily be introduced into the model,

and it is straightforward to show that this would lead to an extension of Eqn (5) to forms such as

$$\frac{\gamma_{(n,C_1^S,C_1^V,C_2^S,C_2^V,\ldots)} - \mu_i C_i^S}{\{\Lambda - \Delta G\}} = h_{(n)} \quad (11)$$

where μ_i would be the chemical potential of component *i* in the unusual units of energy per unit of surface area. This would apply for surface reconstruction or terminations of oxides such as $SrTiO_3$,[117] where the bulk remains as $SrTiO_3$ but the surface composition changes.

It can also be extended to alloys with structures other than FCC. Patala[118] *et al.* indicated that the surface energy is related to the surface stress. Surface stress can be linked to several factors, such as the concentration and molecular weight of surfactants normally present in colloidal syntheses. It is possible that introducing surface stress into calculations will relate segregation to real experimental parameters. This understanding will provide novel opportunities for colloidal synthesis of bimetallic nanoparticles.

The discussion above is only for free standing particles, the analytical studies can be extended to consider particles on substrates as mentioned earlier by including the interface as an extra facet into Winterbottom or Summertop variants of the alloy Wulff construction in Eqn (5).

As a final comment, theoretical models can always match experimental data, but when the amount of experimental data is limited, it can often be ambiguous which models are correct, and which involve inappropriate approximations. The last decade has seen an explosion in the capabilities of electron microscopy, and we are not far from the ability to image all atoms in a 3D structure and identify the chemical nature of each. To improve our understanding of segregation in nanoalloys, we need to have more accurate

hard data, for a range of particle sizes, under carefully controlled experimental conditions. While an understanding of segregation is certainly not trivial, numbers matter and are the route to the future.

6. Acknowledgements

This work was supported by the Materials Research Center (MRSEC) at Northwestern University, on grant number DMR-1121262.

References

1. A. I. Henry, J. M. Bingham, E. Ringe, L. D. Marks, G. C. Schatz and R. P. Van Duyne, *J. Phys. Chem. C*, 2011, **115**, 9291-9305.
2. D. V. Talapin, J. S. Lee, M. V. Kovalenko and E. V. Shevchenko, *Chem. Rev.*, 2010, **110**, 389-458.
3. C. Burda, X. Chen, R. Narayanan and M. A. El-Sayed, *Chem. Rev.*, 2005, **105**, 1025-1102.
4. B. Wiley, Y. Sun and Y. Xia, *Acc. Chem. Res.*, 2007, **40**, 1067-1076.
5. B. R. Cuenya, *Thin Solid Films*, 2010, **518**, 3127-3150.
6. N. E. Motl, E. Ewusi-Annan, I. T. Sines, L. Jensen and R. E. Schaak, *J. Phys. Chem. C*, 2010, **114**, 19263-19269.
7. S. Link, Z. L. Wang and M. A. El-Sayed, *J. Phys. Chem. B*, 1999, **103**, 3529-3533.
8. J. Wilcoxon, *J. Phys. Chem. B*, 2009, **113**, 2647-2656.
9. N. Toshima and T. Yonezawa, *New J. Chem.*, 1998, **22**, 1179-1201.
10. M. Sankar, N. Dimitratos, P. J. Miedziak, P. P. Wells, C. J. Kiely and G. J. Hutchings, *Chem. Soc. Rev.*, 2012, **41**, 8099-8139.
11. H.-L. Jiang and Q. Xu, *J. Mater. Chem.*, 2011, **21**, 13705-13725.
12. C. L. Bracey, P. R. Ellis and G. J. Hutchings, *Chem. Soc. Rev.*, 2009, **38**, 2231-2243.
13. C. J. Murphy, T. K. Sau, A. M. Gole, C. J. Orendorff, J. Gao, L. Gou, S. E. Hunyadi and T. Li, *J. Phys. Chem. B*, 2005, **109**, 13857-13870.
14. J. H. Sinfelt, *Acc. Chem. Res.*, 1977, **10**, 15-20.
15. A. K. Singh and Q. Xu, *Chem. Cat. Chem.*, 2013, **5**, 652-676.
16. X. W. Liu, D. S. Wang and Y. D. Li, *Nano Today*, 2012, **7**, 448-466.
17. C. Wang, M. F. Chi, G. F. Wang, D. van der Vliet, D. G. Li, K. More, H. H. Wang, J. A. Schlueter, N. M. Markovic and V. R. Stamenkovic, *Adv. Funct. Mater.*, 2011, **21**, 147-152.

18. V. R. Stamenkovic, B. S. Mun, K. J. Mayrhofer, P. N. Ross and N. M. Markovic, *J. Am. Chem. Soc.*, 2006, **128**, 8813-8819.
19. J. Suntivich, Z. Xu, C. E. Carlton, J. Kim, B. Han, S. W. Lee, N. Bonnet, N. Marzari, L. F. Allard, H. A. Gasteiger, K. Hamad-Schifferli and Y. Shao-Horn, *J. Am. Chem. Soc.*, 2013, **135**, 7985-7991.
20. L. F. Tan, X. L. Wu, D. Chen, H. Y. Liu, X. W. Meng and F. Q. Tang, *J. Mater. Chem. A*, 2013, **1**, 10382-10388.
21. C. Cui, L. Gan, H. H. Li, S. H. Yu, M. Heggen and P. Strasser, *Nano Lett.*, 2012, **12**, 5885-5889.
22. J. W. Ma, A. Habrioux, T. Miyao, K. Kakinuma, J. Inukai, M. Watanabe and N. Alonso-Vante, *J. Mater. Chem. A*, 2013, **1**, 8798-8804.
23. R. Narayanan and M. A. El-Sayed, *Nano Lett.*, 2004, **4**, 1343-1348.
24. N. Tian, Z. Y. Zhou, S. G. Sun, Y. Ding and Z. L. Wang, *Science*, 2007, **316**, 732-735.
25. K. M. Bratlie, H. Lee, K. Komvopoulos, P. Yang and G. A. Somorjai, *Nano Lett.*, 2007, **7**, 3097-3101.
26. J. Lu, K. B. Low, Y. Lei, J. A. Libera, A. Nicholls, P. C. Stair and J. W. Elam, *Nat. Commun.*, 2014, **5**, 3264.
27. C. J. Serpell, J. Cookson, D. Ozkaya and P. D. Beer, *Nat. Chem.*, 2011, **3**, 478-483.
28. H. Y. Chen, Y. Li, F. B. Zhang, G. L. Zhang and X. B. Fan, *J. Mater. Chem.*, 2011, **21**, 17658-17661.
29. Z. A. Li, M. Spasova, Q. M. Ramasse, M. E. Gruner, C. Kisielowski and M. Farle, *Phys. Rev. B*, 2014, **89**, 161406.
30. S. Stappert, B. Rellinghaus, M. Acet and E. F. Wassermann, *J. Cryst. Growth*, 2003, **252**, 440-450.
31. D. Wang, H. L. Xin, R. Hovden, H. Wang, Y. Yu, D. A. Muller, F. J. DiSalvo and H. D. Abruña, *Nat. Mater.*, 2013, **12**, 81-87.
32. C. Langlois, Z. L. Li, J. Yuan, D. Alloyeau, J. Nelayah, D. Bochicchio, R. Ferrando and C. Ricolleau, *Nanoscale*, 2012, **4**, 3381-3388.
33. Y. Song, K. Liu and S. Chen, *Langmuir*, 2012, **28**, 17143-17152.
34. A. A. Herzing, M. Watanabe, J. K. Edwards, M. Conte, Z. R. Tang, G. J. Hutchings and C. J. Kiely, *Farad. Discuss.*, 2008, **138**, 337-351; discussion 421-334.
35. C. Cui, L. Gan, M. Heggen, S. Rudi and P. Strasser, *Nat. Mater.*, 2013, **12**, 765-771.
36. S. Chen, P. J. Ferreira and Y. Shao-Horn, *Microsc. Microanal.*, 2007, **13**, 604-605.
37. G. Wulff, *Z. Kristallogr. Mineral.*, 1901, **34**, 449-530.
38. M. von Laue, *Z. Kristallogr.*, 1943, **105**, 124-133.
39. A. Dinghas, *Z. Kristallogr.*, 1944, **105**, 304-314.
40. C. Herring, *Phys. Rev.*, 1951, **82**, 87-93.
41. L. D. Marks, *J. Cryst. Growth*, 1983, **61**, 556-566.
42. W. L. Winterbottom, *Acta Metall. Mater.*, 1967, **15**, 303-310.
43. R. K. P. Zia, J. E. Avron and J. E. Taylor, *J. Stat. Phys.*, 1988, **50**, 727-736.
44. E. Ringe, R. P. Van Duyne and L. D. Marks, *Nano Lett.*, 2011, **11**, 3399-3403.

45. L. Vitos, A. V. Ruban, H. L. Skriver and J. Kollar, *Surf. Sci.*, 1998, **411**, 186-202.
46. M. Methfessel, D. Hennig and M. Scheffler, *Appl. Phys. A Mater. Sci. Process.*, 1992, **55**, 442-448.
47. H. H. Kart, M. Tomak and T. Çağin, *Model. Simul. Mater. Sci. Eng.*, 2005, **13**, 657.
48. R. L. Orr, *Acta Metallurgica*, 1960, **8**, 489-493.
49. J. N. Pratt, *Trans. Farad. Soc.*, 1960, **56**, 975-987.
50. L.Vitos, A. V. Ruban, H. L. Skriver and J. Kollar, *Philos. Mag. B*, 1998, **78**, 487-495.
51. H. Y. Wang, R. Najafabadi, D. J. Srolovitz and R. Lesar, *Int. Sci.*, 1993, **1**, 7-30.
52. J. Spreadborough and J. W. Christian, *Journal of Scientific Instruments*, 1959, **36**, 116-118.
53. S. Kristyan and J. Giber, *Surf. Sci.*, 1988, **201**, L532-L538.
54. R. Ferrando, J. Jellinek and R. L. Johnston, *Chem. Rev.*, 2008, **108**, 845-910.
55. S. Heiles and R. L. Johnston, *Int. J. Quantum Chem.*, 2013, **113**, 2091-2109.
56. R. Ferrando, A. Fortunelli and R. L. Johnston, *Phys. Chem. Chem. Phys.*, 2008, **10**, 640-649.
57. M. S. Daw and M. I. Baskes, *Phys. Rev. B*, 1984, **29**, 6443-6453.
58. A. P. Sutton and J. Chen, *Philos. Mag. Lett.*, 1990, **61**, 139-146.
59. R. P. Gupta, *Phys. Rev. B*, 1981, **23**, 6265-6270.
60. M. J. López and J. Jellinek, *J. Chem. Phys*, 1999, **110**, 8899.
61. V. Rosato, M. Guillope and B. Legrand, *Philos. Mag. A*, 1989, **59**, 321-336.
62. F. Cleri and V. Rosato, *Phys. Rev. B*, 1993, **48**, 22-33.
63. R. L. Johnston, *Dalton Trans.*, 2003, 4193-4207.
64. J. P. Perdew and Y. Wang, *Phys. Rev. B* 1992, **45**, 13244-13249.
65. J. Tao, J. P. Perdew, V. N. Staroverov and G. E. Scuseria, *Phys. Rev. Lett.*, 2003, **91**, 146401.
66. V. N. Staroverov, G. E. Scuseria, J. M. Tao and J. P. Perdew, *J. Chem. Phys*, 2003, **119**, 12129-12137.
67. J. P. Perdew, K. Burke and M. Ernzerhof, *Phys. Rev. Lett.*, 1996, **77**, 3865-3868.
68. R. Armiento and A. E. Mattsson, *Phys. Rev. B*, 2005, **72**, 085108.
69. A. E. Mattsson and D. R. Jennison, *Surf. Sci.*, 2002, **520**, L611-L618.
70. J. P. Perdew, A. Ruzsinszky, G. I. Csonka, O. A. Vydrov, G. E. Scuseria, L. A. Constantin, X. Zhou and K. Burke, *Phys. Rev. Lett.*, 2008, **100**, 136406.
71. S. M. Foiles, M. I. Baskes and M. S. Daw, *Phys. Rev. B*, 1986, **33**, 7983-7991.
72. M. I. Baskes, *Phys. Rev. B* 1992, **46**, 2727-2742.
73. D. E. Goldberg, *Genetic Algorithms in Search, Optimization and Machine Learning*, Addison-Wesley Longman Publishing Co., Inc.1989.
74. D. J. Wales and J. P. K. Doye, *J. Phys. Chem. A*, 1997, **101**, 5111-5116.
75. L. Deng, W. Hu, H. Deng, S. Xiao and J. Tang, *J. Phys. Chem. C*, 2011, **115**, 11355-11363.
76. L. Deng, W. Hu, H. Deng and S. Xiao, *J. Phys. Chem. C*, 2010, **114**, 11026-11032.
77. D. Zhiyao and W. Guofeng, *J. Phys. Condens. Matter*, 2011, **23**, 475301.
78. G. Wang, M. A. Van Hove, P. N. Ross and M. I. Baskes, *J. Chem. Phys.*, 2004, **121**, 5410-5422.

79. G. Wang, M. A. Van Hove, P. N. Ross and M. I. Baskes, *J. Phys. Chem. B*, 2005, **109**, 11683-11692.
80. G. Wang, M. Vanhove, P. Ross and M. Baskes, *Prog. Surf. Sci.*, 2005, **79**, 28-45.
81. F. Baletto, C. Mottet and R. Ferrando, *Phys. Rev. Lett.*, 2003, **90**, 135504.
82. C. T. Campbell, *Acc. Chem. Res.*, 2013, **46**, 1712-1719.
83. O. S. Alexeev and B. C. Gates, *Ind. Eng. Chem. Res.*, 2003, **42**, 1571-1587.
84. J. B. Park, S. F. Conner and D. A. Chen, *J. Phys. Chem. C*, 2008, **112**, 5490-5500.
85. A. Aguado, in *Nanoalloys*, ed. F. Calvo, Elsevier, Oxford2013, pp. 75-111.
86. F. R. Negreiros, G. Barcaro, Z. Kuntova, G. Rossi, R. Ferrando and A. Fortunelli, *Surf. Sci.*, 2011, **605**, 483-488.
87. R. Ismail, R. Ferrando and R. L. Johnston, *J. Phys. Chem. C*, 2013, **117**, 293-301.
88. X. Xiang, J. Nie, K. Sun, L. Zhang, W. Liu, J. Schwank, S. Wang, M. Zhong, F. Gao and X. Zu, *Nanoscale*, 2014, **6**, 12898-12904.
89. S. J. Pennycook and D. E. Jesson, *Ultramicroscopy*, 1991, **37**, 14-38.
90. A. Howie, *J. Microsc.*, 1979, **117**, 11-23.
91. J. Llorca, M. Dominguez, C. Ledesma, R. Chimentao, F. Medina, J. Sueiras, I. Angurell, M. Seco and O. Rossell, *J. Catal.*, 2008, **258**, 187-198.
92. R. He, Y. C. Wang, X. Wang, Z. Wang, G. Liu, W. Zhou, L. Wen, Q. Li, X. Wang, X. Chen, J. Zeng and J. G. Hou, *Nat. Commun.*, 2014, **5**, 4327.
93. T. A. Silva, E. Teixeira-Neto, N. Lopez and L. M. Rossi, *Sci. Rep.*, 2014, **4**, 5766.
94. S. Cheong, L. Graham, G. L. Brett, A. M. Henning, J. Watt, P. J. Miedziak, M. Song, Y. Takeda, S. H. Taylor and R. D. Tilley, *Chem. Sus. Chem*, 2013, **6**, 1858-1862.
95. H. M. Song, B. A. Moosa and N. M. Khashab, *J. Mater. Chem.* , 2012, **22**, 15953-15959.
96. R. Wang, Z. Wu, C. Chen, Z. Qin, H. Zhu, G. Wang, H. Wang, C. Wu, W. Dong, W. Fan and J. Wang, *Chem. Commun.*, 2013, **49**, 8250-8252.
97. W. G. Menezes, B. Neumann, V. Zielasek, K. Thiel and M. Bäumer, *Chem. Phys. Chem.*, 2013, **14**, 1577-1581.
98. W. Tao, M. Junkui, W. Xingrui, L. Yue, X. Han, G. Jianping, W. Wei, L. Yu and Y. Jing, *Nanotechnology*, 2013, **24**, 125301.
99. D. B. Williams and C. B. Carter, *Transmission Electron Microscopy*, Plenum Pr, New York, 1996.
100. A. Genc, L. Kovarik, M. Gu, H. Cheng, P. Plachinda, L. Pullan, B. Freitag and C. Wang, *Ultramicroscopy*, 2013, **131**, 24-32.
101. L. D. Marks and D. J. Smith, *J. Cryst. Growth*, 1981, **54**, 425-432.
102. D. J. Smith and L. D. Marks, *J. Cryst. Growth*, 1981, **54**, 433-438.
103. D. J. Smith and L. D. Marks, *Philos. Mag. A*, 1981, **44**, 735-740.
104. L. D. Marks and D. J. Smith, *Nature*, 1983, **303**, 316-317.
105. U. Dahmen, R. Erni, C. Kisielowki, V. Radmilovic, Q. Ramasse, A. Schmid, T. Duden, M. Watanabe, A. Minor and P. Denes, in *EMC 2008 14th European Microscopy Congress 1–5 September 2008, Aachen, Germany*, eds. M. Luysberg, K. Tillmann and T. Weirich, Springer Berlin Heidelberg2008, ch. 2, pp. 3-4.
106. D. Pohl, U. Wiesenhutter, E. Mohn, L. Schultz and B. Rellinghaus, *Nano Lett.*, 2014, **14**, 1776-1784.

107. Y. Wu, D. Wang, Z. Niu, P. Chen, G. Zhou and Y. Li, *Angew. Chem. Int. Ed. Engl.*, 2012, **51**, 12524-12528.
108. C. Chen, Y. Kang, Z. Huo, Z. Zhu, W. Huang, H. L. Xin, J. D. Snyder, D. Li, J. A. Herron, M. Mavrikakis, M. Chi, K. L. More, Y. Li, N. M. Markovic, G. A. Somorjai, P. Yang and V. R. Stamenkovic, *Science*, 2014, **343**, 1339-1343.
109. B. G. Bagley, *Nature*, 1965, **208**, 674-675.
110. C. Y. Yang, *J. Cryst. Growth*, 1979, **47**, 274-282.
111. S. Ino, *J. Phys. Soc. Jpn.*, 1969, **27**, 941-953.
112. L. D. Marks, *Philos. Mag. A*, 1984, **49**, 81-93.
113. R. d. Wit, *J. Phys. C: Solid State Phys.*, 1972, **5**, 529.
114. V. Volterra, *Ann. Scient. Ec. Norm. Sup.*, 1907, **24**, 401.
115. A. Howie and L. D. Marks, *Philos. Mag. A*, 1984, **49**, 95-109.
116. L. Peng, R. P. van Duyne and L. D. Marks, *Submitted*, 2015.
117. Y. Lin, J. Wen, L. Hu, R. M. Kennedy, P. C. Stair, K. R. Poeppelmeier and L. D. Marks, *Phys. Rev. Lett.*, 2013, **111**, 156101.
118. S. Patala, L. D. Marks and M. O. de la Cruz, *J. Phys. Chem. Lett.*, 2013, **4**, 3089-3094.